

Landslides (2022) 19:637–646  
 DOI 10.1007/s10346-021-01818-y  
 Received: 5 October 2021  
 Accepted: 1 December 2021  
 Published online: 19 January 2022  
 © The Author(s) 2021

Che-Ming Yang · Jui-Ming Chang · Chi-Yao Hung · Chih-Heng Lu ·  
 Wei-An Chao  · Keng-Hao Kang



## Life span of a landslide dam on mountain valley caught on seismic signals and its possible early warnings

**Abstract** Outburst flooding after a landslide dam breach causes global fatalities and devastation. Information on the timing, magnitude, and location of the landslide dam is crucial to hazard assessment. Despite recent efforts, successful real-time detection of landslide dams in mountain valleys and dam breakages is rare. Here, we present a series of seismic analysis including landslide detection, identification of landslide dam formations, and monitoring of dam breaches. We show the working of our analysis on a recent landslide dam that occurred in eastern Taiwan. The results indicate that our seismic analysis provides important information on the location and magnitude of landslides and the dam forming based on data acquired from a regional broadband seismic network. Furthermore, we see that the failure of the landslide dam is directly caught by the riverside seismic signals. To provide warning times for impending floods to downstream areas, we believe that proximal high-quality seismic signals along the river channel are viable options for an operational real-time monitoring system, for landslide dams occurring in mountain valleys. Our work can be a starting point to raise awareness in the community.

**Keywords** Landslide dam · Seismic signals · Warning times · Impending floods

### Introduction

Catastrophic outburst of debris flows or flooding due to dam failures can lead to serious damage and inundation of downstream areas near rivers. In such scenarios, the response time available to warn the populace is a critical issue for hazard mitigation and emergency response. To capture the time of occurrence of the water overflow, a conventional method is to install a water gauge station to monitor the water stage of the ponding water behind the landslide dam. However, it is very difficult to establish an in situ monitoring system for water gauges because landslides usually occur in rugged mountain areas. Owing to the aforementioned difficulties, a fully documented landslide dam breach process is lacking. In the database (the total number of landslide dams of 1,237) of Peng and Zhang (2012), 4% of the landslide dam cases had only an estimated information of dam breaching. Only six cases have complete recordings of the breaching process, which can be found in the historical global database (Lee and Duncan 1975; Umbal and Rodolfo 1996; Capart et al. 2007; Liu et al. 2010). The limitation in recording dam failure details causes difficulties in validating the physical-based numerical model. Physical modeling is sometimes time-consuming and is thus not suitable for emergency responses. Thus, Peng and Zhang (2012) pointed out that crucial parameters

such as the dam geometry (height, width, length, and volume) and the impoundment catchment area can be used for rapid assessment of landslide dam stability after the dam formation. In the past two decades, numerous parametric breach models have been developed. Wu et al. (2011) summarized the models proposed in the literature and conducted a series of laboratory experiments to verify the models. In addition, a few studies proposed empirical regression models based on field-based observations (Walder and O'Connor 1997; Ermini and Casagli 2003; Dong et al. 2011; Fan et al. 2019). In practice, the aforementioned dam information can be investigated using an unmanned aerial vehicle (UAV) and satellite optical images. However, remote sensing data are not always available in mountainous areas with deep and narrow valleys, leading to poor time resolution in understanding landslide dams. A possible solution to overcome this monitoring difficulty is to adopt seismic techniques. Seismic signals have successfully been applied to study the landslide source dynamics (Allstadt 2013; Yamada et al. 2013; Chao et al. 2017; Chang et al. 2021; Weng et al. 2021), river sediment transport (Schmandt et al. 2013; Chao et al. 2015; Gimbert et al. 2019), early identification of dam formation (Chao et al. 2016), early warning of landslides (Poli 2017; Schöpa et al. 2018), and debris flow mechanics (Walter et al. 2017; Lai et al. 2018). Deposit recent efforts in landslide seismology, we still lack a monitoring framework to completely trace the seismic signatures for detecting and locating the landslide, identifying the dam formation, and providing early warning for impending floods.

A landslide dam formed on February 4, 2021, was used to validate and demonstrate our proposed seismic framework for detecting and monitoring landslide dam breaching. The impact areas of possible impending outburst floods are a hydroelectric power plant, roads beside the river flow path, and an irrigation canal. The hydroelectric power plant is located in Tongxin village in Taitung, which was first operated in eastern Taiwan to provide electricity in early 1945. The canal is a very important artificial channel for carrying water from the Danan River to the fields around Tongxin village to perform irrigation (Fig. 1a). Considering the impact areas, three seismic stations equipped with one highly sensitive broadband velocity-type seismometer (DALB) and two geophones (DALU, DALD) were installed after landslide dam formation and continuously monitored until their failure. Station DALB was deployed on the top of a mountain with a horizontal distance of 1.64 km from river-to-station and an elevation of 650 m relative to the riverbed. Stations DALU and DALD (riverside stations) were installed within 200 m of the river channel (Fig. 1). Real-time data streams of stations of DALB and DALD are available via the seedlink server,

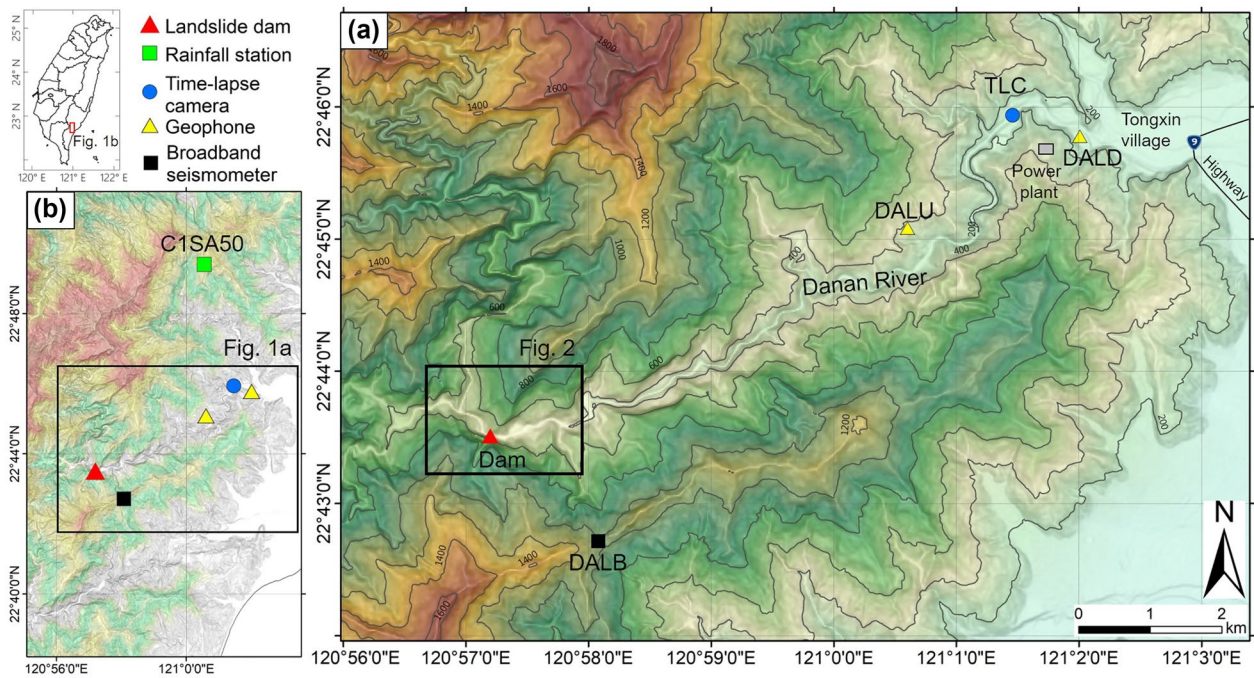


**Fig. 1** **a** Topographic map (coordinate system: TWD 1997 TM Taiwan). The Tongxin power plant, village, and highway (no. 9) located downstream of the Danan River. **b** Regional map shows the distribution of monitoring stations and the location of rain gauge

which would enable us to provide timely warnings of dam breaching and have the potential to mitigate any loss of life.

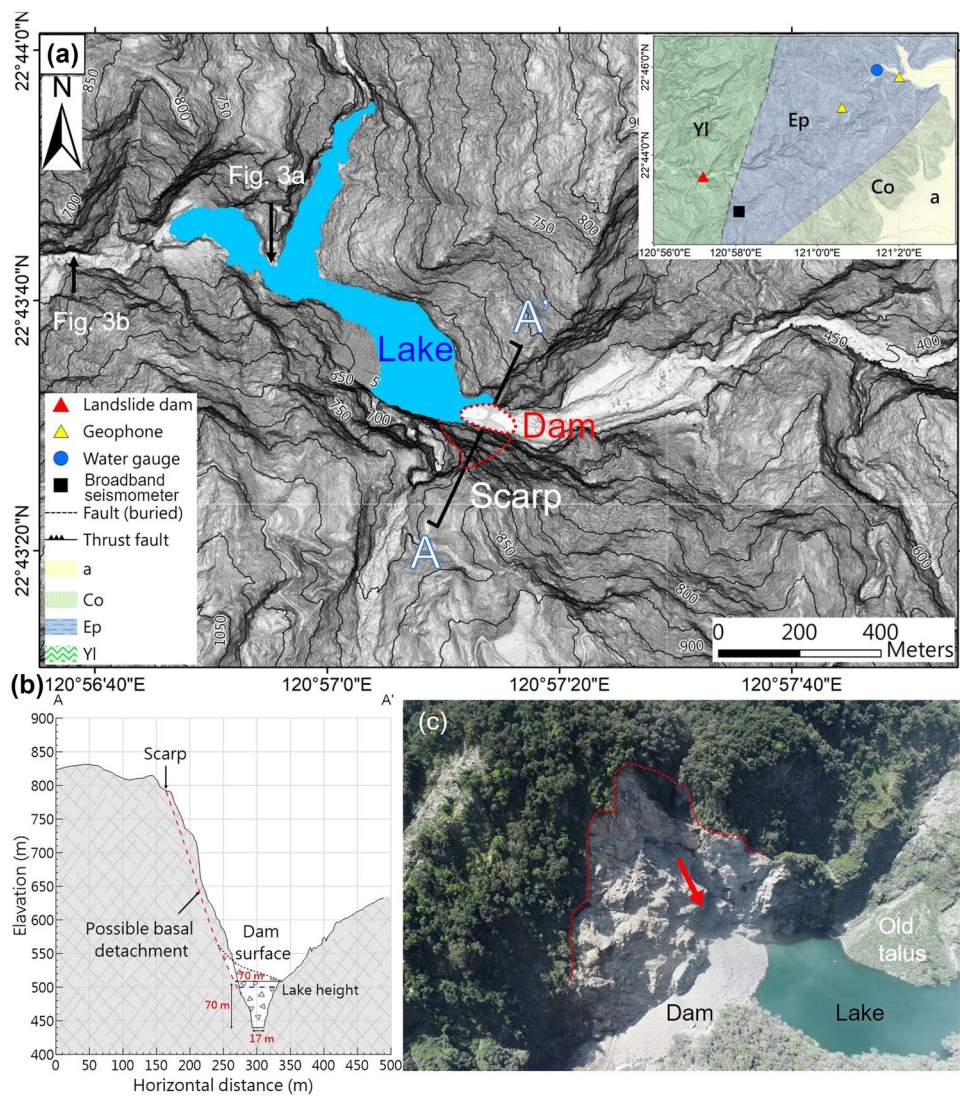
#### Formation of landslide dam and its evolution

The Danan landslide dam and breach occurred on February 4 and August 7, 2021, respectively, due to a steep rock slope collapse. The collapsed rock slope, located at  $22.724364^{\circ}\text{N}$  and  $120.952677^{\circ}\text{E}$ , belongs to the Yuli Formation (YI) of the Tananao schist (Fig. 2a). YI is mainly composed of black schists with occasional thin and thick meta-sandstone. The thickness of the meta-sandstone varies from several centimeters to tens of meters (Fei and Chen 2013; Yang et al. 2020). Profile AA' (Fig. 2b) shows the topographic profile by 2012 light detection and ranging digital elevation model (LiDAR DEM) and infers the possible basal detachment and the landslide dam using aerial photos (Fig. 2c). This aerial photo of the source region was captured from a helicopter immediately after dam formation. The base elevation of the landslide dam is approximately 440 m above the sea level (asl). The dammed lake surface roughly follows a contour line of 500 m asl. The estimated height of the landslide dam is approximately 70 m. The top and bottom widths of the landslide dam are approximately 70 m and 17 m, respectively. Assuming a landslide dam length of 100 m and trapezoidal shape in profile AA', the estimated volume of the landslide dam is  $304,500\text{ m}^3$ . In addition, the steep collapsed rock slope faces north and exposes the light color bedrock with a rugged surface (Fig. 2c). The shapes of the boulder and debris are blocky and granular rather than flake or platy, indicating that the lithology must be identified as a thick meta-sandstone with a blocky structure. A high elevation difference of the knick point, buried by the dammed lake, leads to difficulties in field surveys and in deployment of monitoring instruments

around the collapse area (Fig. 3a). However, we observed that the outcrop of folded meta-sandstone is exposed along the Danan River (Fig. 3b), which is similar to the outcrop of the collapsed rock slope. In addition, a large old talus and exposed outcrops of steep slopes also indicate that the events of rockfall and massive mass collapse occur frequently in this region (Figs. 3c, d).

Quantitative data on the impoundment catchment area and dam geometry are crucial for studying the relationships between dam evolution and external forces (e.g., earthquake-induced ground shaking and precipitation), and to recognize potential causes of dam failure. Here, we collect time-lapse remote sensing data: Sentinel-1 synthetic aperture radar (SAR) images and Sentinel-2 optical images. The Sentinel-1 satellite, launched by the European Space Agency (ESA), carries a C-band SAR sensor with 6–12 days repeat scan cycle. The raw data are calibrated by ESA to produce a ground range detected high (GRDH) type with a spatial resolution of 10 m. The microwave of SAR can penetrate through clouds, which has been applied to map flooding in urban areas successfully (Mason et al. 2010, 2014; Giustarini et al. 2013). Theoretically, the water surface is ideal to reflect the microwaves into the opposition, resulting in a dark area in the amplitude image (see the February 25 SAR image shown in Fig. 4). However, the side-looking observation system of SAR satellites is limited by the geometry of the satellite altitude and the surface target (Hanssen 2001). The terrain effects, including foreshortening, layover, and shadow, would affect the water mass detection of a river channel in a mountainous area. In contrast, the optical images of the Sentinel-2 satellite from ESA can provide independent constraints on the impoundment catchment area but cannot be used because of cloud coverage and cloud shadows.

**Fig. 2** **a** High-resolution LiDAR slope map shows collapsed rock slope, landslide dam, dammed lake, and line of profile AA'. Illustration (top-right) is regional geological map (identical area with Fig. 1a) that includes strata and geological structures. Yl: Late Paleozoic to Mesozoic Yuli Formation; Ep: Eocene Pilushan Formation; Co: Middle Miocene Chaochou Formation; a: Holocene alluvium. **b** Topographic profile AA'. **c** Landslide, scarp, natural dam, and dammed lake. Arrow indicates the collapse direction



Here, we propose a joint analysis of multi-temporal data from optical and SAR images, to comprehensively provide the temporal changes in the highest elevation of the dammed lake surface ( $H_L$ ). First, the available optical images and the digital terrain model (DTM) with resolution of 20 m, from the Department of Land Administration, Ministry of the Interior, Taiwan, are capable of providing direct evidence of  $H_L$ . Then, following the approaches proposed by Clement et al. (2018) and Uddin et al. (2019), the specific image features in SAR for identifying  $H_L$  can be extracted by fitting the  $H_L$  values derived from optical images. The above features are directly applied to the data with only SAR images. Figure 4 shows the time series of  $H_L$  extracted from satellite images, which increased from 465 to 518 m asl as expected, and then dropped to 469 m asl (August 12, Fig. 4) rapidly after dam breaching. Notably, the riverbed widened from 96 m (July 09) to 162 m (August 18), as depicted by the yellow arrows in Fig. 4. Assuming that the dimensions of the deposited materials are 162 m in width, 400 m in longitudinal length along the river, and 2 m in thickness, the total volume of deposits of 129,600 m<sup>3</sup> can be estimated, which is half of the landslide dam volume. This implies that the dam was

partially breached. The lake still exists today and is visible in optical images from August 18 (Fig. 4, 463 m asl at the top of the remaining lake). There is a discrepancy in  $H_L$  estimated from SAR and optical images. Overall, the SAR results show underestimated values compared with the optical results. The limitation might come from the atmospheric effects that influence the intensity of the radar signals received and could cause difficulty in picking lake surface signals near the shadow or layover area, via the influenced amplitude image, precisely. Even so, the continued observational ability of SAR images can play a key role in acquiring important surface information under worse weather conditions.

Here, we present an investigation of the impact of external forcing on the variances in  $H_L$  values. Overall, a series of the highest elevations of the dammed lake surface was strongly sensitive to rainfall episodes and should be mainly controlled by rainfall-runoff behavior (Fig. 5). Rainfall data recorded at a rain gauge station of C1SA50 operated by the Central Weather Bureau, Taiwan (CWB) (Fig. 1b), which is 12.4 km away from the landslide dam. The predicted peak ground acceleration (PGA shown in Fig. 5) at the landslide site was estimated using the ground motion prediction



**Fig. 3** **a** A knick point (vertical arrow) at upstream of Danan River (view from upstream). **b** Outcrop of folded meta-sandstone along left bank of Danan River. **c** Collapsed rock slope, dammed lake, and

old talus (view from upstream). **d** Dam and downstream river bed (view from downstream)

**Fig. 4** Sentinel satellite images exhibit the process from pre-collapse to dam breaching. White arrows indicate the location of landslide dam, blue arrows show the highest elevation of dammed lake, and yellow arrows point out the width change before and after dam breaching. The optical image at August 18 indicates the length and width of deposits by dam breaching

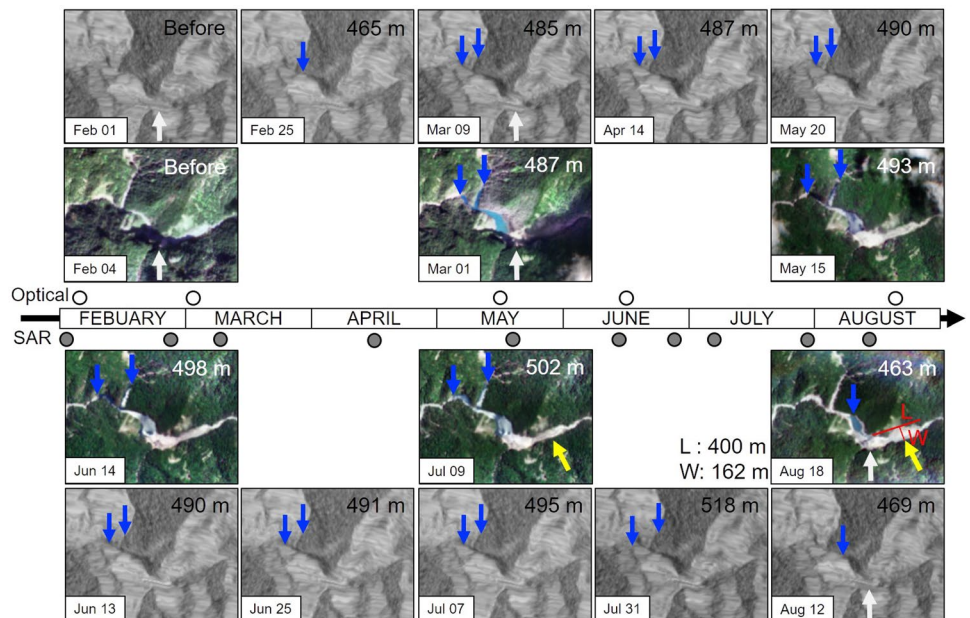
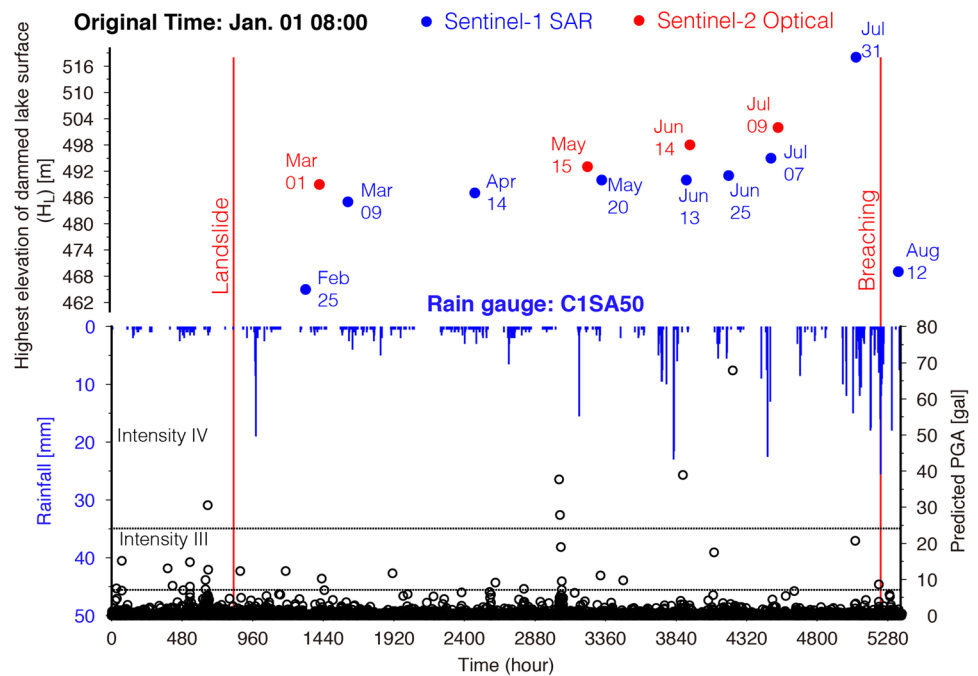


**Fig. 5** Time series of highest elevation ( $H_L$ ) (red circles: optical; blue circles: SAR), predicted PGA and hourly precipitation. Red vertical lines are the timings of landslide occurrence and dam breaching caught on the seismic signals



equation (GMPE, Lin et al. 2011). However, the temporal resolution of satellite images is insufficient to discuss the interaction between earthquake forcing and dam evolution.

## Results and discussion

### Seismic detection of the landslide dam

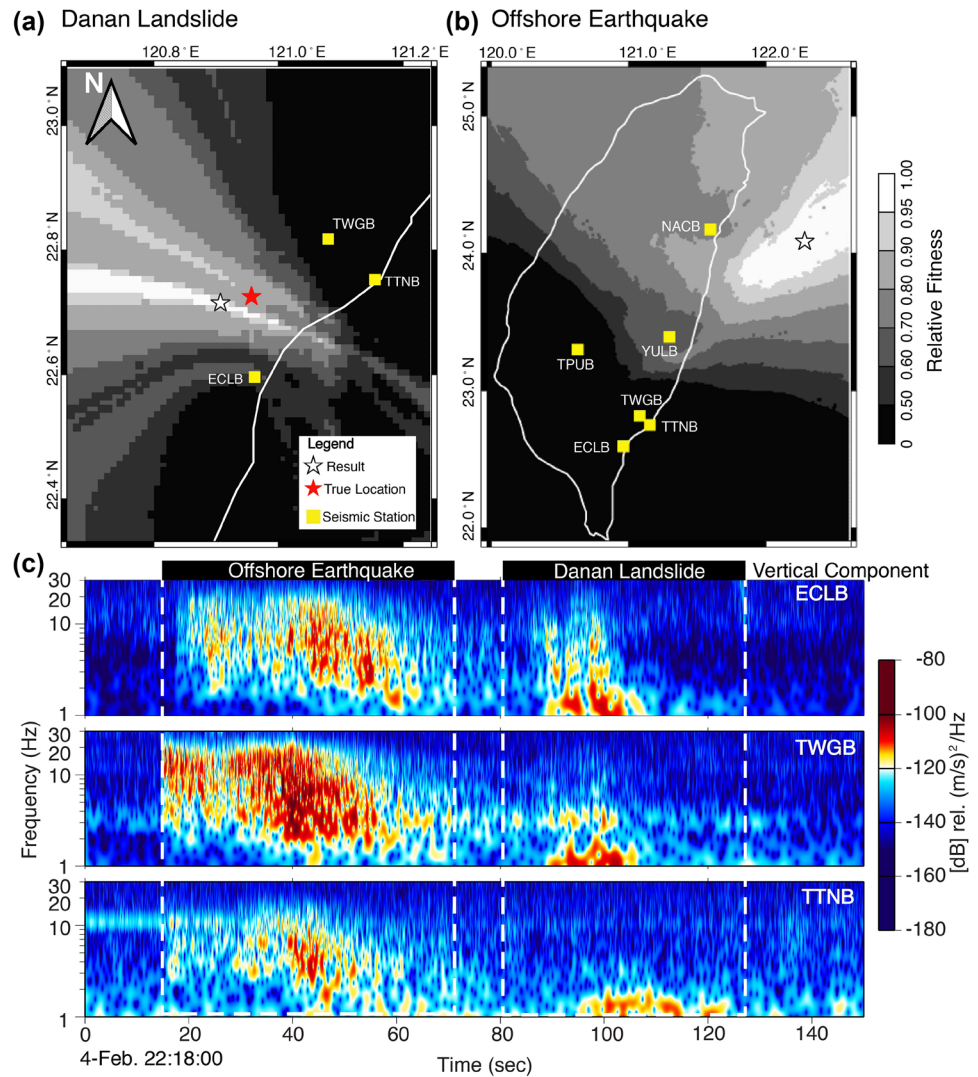
Early identification of landslide dam formation is a challenge, but it is required for an emergency response. In the present study, we first utilized a flexible approach of seismic source scanning (GeoLoc scheme referred in Chang et al. 2021) to detect seismic signals induced by landslides and locate its possible location. In the GeoLoc scheme, only stations with signal-to-noise ratios higher than 1.5 are used in the location processing. Using 2-days (4–5 August) continuous seismic records from six regional broadband stations and a band-pass filtering of 1–5 Hz, a total of 22 events were detected automatically, and 16 of them were listed in the earthquake catalog reported by the CWB. Recent studies demonstrated that seismic signals associated with landslides have a ratio less than 0.80–0.85 that is between local magnitude ( $M_L$ ) and duration magnitude ( $M_D$ ) (Chang et al. 2021; Manconi et al. 2016). To discriminate between the source types of detected events, we carefully examined the magnitude ratios of  $M_L/M_D$  for the detected events excluded from the CWB earthquakes. Consequently, an event with a  $M_L/M_D$  value of 0.84 occurred on February 4, 2021 at 22:19:20 (local time), which is associated with the Danan landslide. The  $M_L$  and  $M_D$  of the landslide were 1.68 and 1.98, respectively. The estimated location is approximately 5.24 km away from the field location (Fig. 6a). The above error in location estimation can be improved by using the better azimuthal distribution of seismic stations. According to the empirical law ( $\text{Log}_{10}[\text{Volume}] = 1.12 M_L + 3.08$ ) for source volume estimation reported by Chang et al. (2021), the landslide volume is approximately 91,537 m<sup>3</sup>, which is roughly consistent with the dam volume inferred from images, if we consider a landslide dam

porosity of 0.5. One detected event with an  $M_L/M_D$  value of 1.10, which occurred before the Danan landslide, was an offshore earthquake reported by the CWB (Fig. 6b). Figure 6c shows the discrepancies in the time–frequency characteristics between the landslide and the offshore earthquake. Notably, at the station closest to the ECLB for the Danan landslide, a pulse-like shape in spectrograms with a frequency ranging from 1 to 10 Hz (Fig. 6c) is generated by the collapsed mass detached from the steep hillslope, impacting the riverbed, and further blocking the river channel, which cannot be observed at a farther station (TTNB with an epicentral distance of ~21 km). The aforementioned observations are similar to the seismic dam-forming phase (D-phase) reported by Chao et al. (2016). The signal duration of 23.54 s would correlate with the event duration (Chen et al. 2013).

### Seismic monitoring of dam breach

The standard method for quantifying the time and frequency characteristics of seismic noise is to compute the power spectral density (PSD) of seismic signals (McNamara and Buland 2004). For our analysis, we first cut continuous vertical component seismic records into 1-h time series segments that overlap by 50%. Each 1-h waveform is divided into 15-min moving windows with 75% overlap, and fast Fourier transform (FFT) is applied to compute the spectral amplitudes (Welch 1967). The PSD is the square of the spectral amplitude with a normalization factor. The PSD estimate for each 1-h segment was computed by averaging the PSDs of all 15-min waveforms. The spectrogram of DALB shown in Fig. 7 exhibits a strong PSD excited by the teleseismic event, local earthquakes, and microseisms. Microseisms (primary and secondary) are primarily induced by interactions between ocean waves and the seafloor (McNamara and Buland 2004). In contrast to the broadband station of the DALB, station DALD (geophone sensor at the riverside) can only record the local earthquake signals and show a clear diurnal

**Fig. 6** Location results of **a** the offshore earthquake and **b** the Danan landslide determined by the GeoLoc scheme. **c** Spectrograms of ECLB, TWGB, and TTNB. Vertical white dash lines indicate the signal windows associated with the earthquake and landslide. Colors indicate the power spectral density (PSD)



pattern caused by human activity. The data from station DALU were not usable because of GPS antenna problems. Both stations (DALB and DALD) reveal relatively high-frequency signals (black rectangles shown in Fig. 6), which were correlated to the landslide dam burst. Furthermore, we focused on the precipitation and seismic activity over a period of 19 days before dam failure (Fig. 5). Low ground shaking was clearly observed, and most likely only two earthquakes with CWB intensity III affected the landslide area. The antecedent precipitation with prolonged and heavy rainfall implies that overtopping caused by water spilling over the top of a dam is a major failure mode for this landslide dam.

For a better understanding of the seismic signatures related to dam breaching, we further parse continuous seismic records into 3-h-length waveforms with a starting time point of AM 06:30, August 7 (local time). Similar to the aforementioned analysis of the PSD estimate, we cut 3-h-length waveforms into 3-min data segments that overlap by 50%. Each 3-min record is divided into 15-s moving windows with 75% overlap to improve the time resolution of the spectrogram. Figure 8 shows the PSD as a function of frequency for the specific time stages and spectrograms, which would be helpful to see the variance in amplitude and frequency

for different stages. Overall, a clear strong PSD with frequency content higher than 2 Hz can be observed in station DALD (Fig. 8b). In contrast to station DALD, station DALB exhibits a weak PSD with an exciting frequency below 10 Hz (Fig. 8a). These discrepancies can contribute to the attenuation effect of the seismic wave propagation. The propagation distance of station DALB is larger than that of station DALD. To quantify the evolution of leading signals (possible warning time), we first selected the PSD curve at time point  $t_0$  as reference (background noise level, open circles shown in Fig. 8). Secondly, the maximum PSD differences (mPSD; blue dots in Fig. 8) between the representative and reference PSD curves were calculated for each specific time point. By considering a threshold of mPSD of 4 dB, we picked up the time points  $t_1$  and  $t_6$  for stations of DALB and DALD, respectively, which correspond to the dam breaching and rapid transport of sediment pulse and water flooding. A threshold of 4 dB was determined manually based on the background noise level of the seismic station, which will be evaluated in future studies. The seismic signals recorded at station DALB lying close enough to the landslide dam can provide the possibility of understanding the behavior of dam failure and outburst flooding. For example, a gradual increase in mPSD

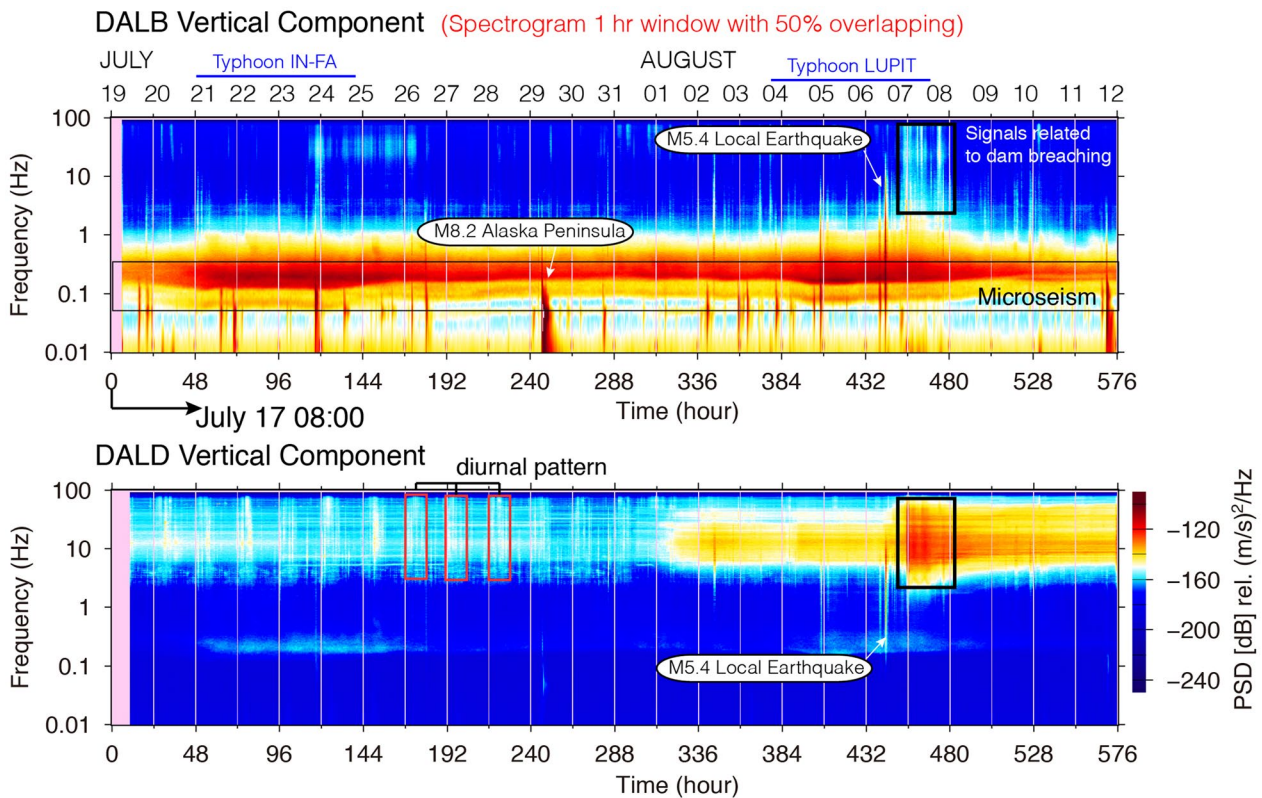


**Fig. 7** Spectrograms of stations DALB (top) and DALD (middle). Black rectangles are the seismic signals related to dam breaching and microseism, respectively. Red rectangles relate to the human activ-

ity, exhibiting the diurnal pattern in spectrogram. Colors indicate the power spectral density (PSD)

during period— $t_1$ – $t_2$  corresponds to water overtopping, and the dam would start to breach. After the  $t_2$ -time-point, the increases in mPSD amplitudes indicate the sudden collapse of dam materials, developing the breach crest, and then material mixtures of sediment and water approach the seismic station. Strong mPSD amplitudes around the  $t_3$ -time-point with a duration of approximately 30 min correspond to an outflow with strong flow dynamics. The PSD curve at  $t_3$ -time-point shown in Fig. 8a (black lines) is an example of PSD during the strong water stage. Finally, the mPSD amplitudes decreased after the peak water stage (see two time points of  $t_4$  and  $t_5$  in Fig. 8a). Moreover, the outburst flooding image near station DALD was captured at AM 07:35:57, August 7 (local time), which is exactly after the duration of dramatic increase between time points of  $t_7$  and  $t_8$  (Fig. 51a). The time of seismic signal of station DALD should be detected earlier than the in situ image of camera, which also implies that the seismic power of station DALD can provide an indirect observation of the water stages. Notably, the PSD curve and mPSD of station DALD after the  $t_8$ -time-point (Fig. 8b) cannot return to the background noise level due to the artificial control of the water gate.

#### Was an early warning possible for dam breach

To provide early operational warnings for imminent flooding after dam breaching, we compute the onsite early warning time

of 10.5 min (time difference between  $t_2$  and  $t_1$ ) and 45 min (time difference between  $t_7$  and  $t_6$ ) for stations DALB and DALD, respectively (Fig. 8). For an operation of regional early warning, we need to collect and analyze seismic signals from a station located upstream and provide warnings to the downstream site. In our case, we could have enabled a warning time of 33 min ( $t_7$ -time-point minus  $t_2$ -time-point) before the arrival of the impending floods. Considering a station-to-station distance of 11.4 km along the river channel, an apparent flow velocity of 5.8 m/s can be estimated. A peak water discharge of  $\sim 2,274 \text{ m}^3/\text{s}$  can also be estimated by using the peak water depth of 7 m and channel width downstream of 56 m (Fig. 51b).

#### Limitations in seismic monitoring framework

In fact, inaccuracy in determining landslide location and real-time detection of dam breach are two critical issues in our current framework. To reduce the uncertainties in source location, the additional seismic stations around the landslide area with high potential failure are required. A threshold of mPSD of 4 dB was directly applied for the identification of the starting time point of dam breaching. However, this specific threshold should be depended on the instrument type, site condition, and background noise level. Thus, how to select a proper early warning threshold to detect dam failure is a major argument. Recently, a significant

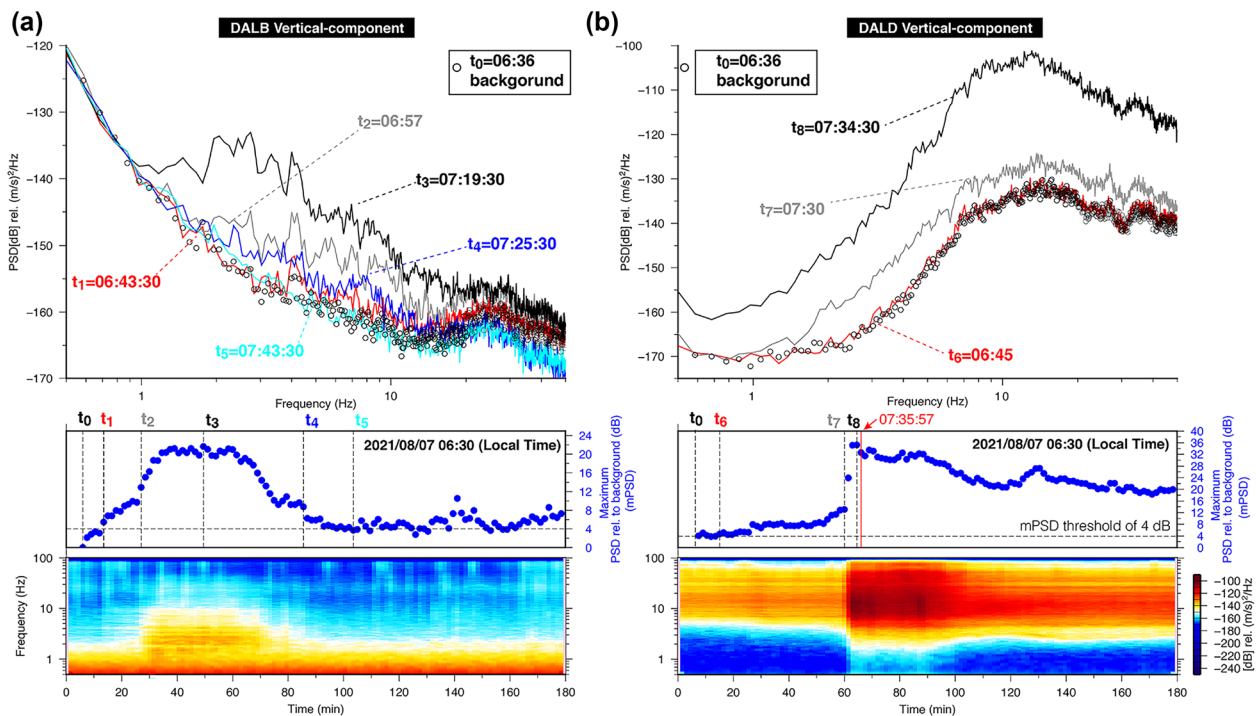


**Fig. 8** Power spectrums of difference time stages, maximum power spectral density relative to reference PSD (mPSD), and spectrograms of **a** DALB and **b** DALD. Vertical dashed lines depict the specific time

points. Horizontal dashed line indicates the threshold of 4 dB of mPSD for issuing the warnings. Vertical red line indicates the time point for the image of CCTV shown in Figure S1a

research effort has been made for real-time signal detection using machine-learning technologies (Chin et al. 2020). Using the suitable machine-learning scheme, the seismic signals of dam breaching, ambient noise, and earthquake can be used as the features to train the model, which advances the detection performance for practical real-time data stream. These potential solutions for the aforementioned issues have to be tested in future studies. In addition, we also propose a jointly analyzing data acquired from seismic stations and satellite images to comprehensively understanding the evolution of landslide dam.

## Conclusions

Our study presents a seismic framework that includes detecting and locating landslides, identifying dam forming. A warning threshold of 4 dB mPSD was adopted in this study, which has the potential to provide timely warning of imminent flooding that could save many lives.

After dam breaching, most of the dam material was deposited at the front of the dam (optical images on August 18, shown in Fig. 4). The remaining dammed lake increased slightly with subsequent precipitation. The aforementioned condition highlights the possible risks related to hazards caused by dam breaching. For accuracy and to avoid false alarms for warnings, we need proper seismic networks to consist of highly sensitive

seismometers near the river channel with good azimuthal coverage.

## Acknowledgements

The authors acknowledge the Forestry Bureau, Council of Agriculture, Executive Yuan, Taiwan, for providing aerial photos and camera photo. The authors also acknowledge the CWB for the earthquake inventory, rainfall data, and seismic records and the Institute of Earth Science (IES) of Academia Sinica, Taiwan, for the broadband waveforms. Satellite images used in this work are available from BigGIS (<https://gis.swcb.gov.tw/>).

## Funding

This research was supported by the Ministry of Science and Technology (MOST), Taiwan, grant MOST 110-2636-M-009-001 (the Young Scholar Fellowship Einstein Program) and MOST 110-2124-M-027-001, and partially supported financially by the Academia Sinica grant AS-TP-109-M08; the Central Geological Survey, Taiwan (grant no. B11018); and the Soil and Water Conservation Bureau, Taiwan (grant no. SWCB-110-031).

## Declarations

**Conflict of interest** The authors declare no competing interests.



**Open Access** This article is licensed under a Creative Commons Attribution 4.0 International License, which permits use, sharing, adaptation, distribution and reproduction in any medium or format, as long as you give appropriate credit to the original author(s) and the source, provide a link to the Creative Commons licence, and indicate if changes were made. The images or other third party material in this article are included in the article's Creative Commons licence, unless indicated otherwise in a credit line to the material. If material is not included in the article's Creative Commons licence and your intended use is not permitted by statutory regulation or exceeds the permitted use, you will need to obtain permission directly from the copyright holder. To view a copy of this licence, visit <http://creativecommons.org/licenses/by/4.0/>.

## References

- Allstadt K (2013) Extracting source characteristics and dynamics of the August 2010 Mount Meager landslide from broadband seismograms. *J. Geophys. Res.* 118:1472–1490
- Capart H, Spinewine B, Young DL et al (2007) The 1996 Lake Ha! Ha! breakout flood, Québec: test data for geomorphic flood routing methods. *J Hydraulic Research* 45:97–109
- Chang JM, Chao WA, Chen H, Kuo YT, Yang CM (2021) Locating rock slope failures along highways and understanding their physical processes using seismic signals. *Earth Surf Dynam* 9:505–517. <https://doi.org/10.5194/esurf-9-505-2021>
- Chao WA, Wu YM, Zhao L, Tsai VC, Chen CH (2015) Seismologically determined bedload flux during the typhoon season. *Sci Rep* 5:8261. <https://doi.org/10.1038/srep08261>
- Chao WA, Zhao L, Chen SC et al (2016) Seismology-based early identification of dam-formation landslide events. *Sci Rep* 6:1–7. <https://doi.org/10.1038/srep19259>
- Chao WA, Wu YM, Zhao L et al (2017) A first near real-time seismology-based landslide monitoring system. *Sci Rep* 7:1–12. <https://doi.org/10.1038/srep43510>
- Chen CH, Chao WA, Wu YM et al (2013) A seismological study of earthquakes using a real-time broadband seismic network. *Geophys J Int* 194:885–898. <https://doi.org/10.1093/gji/ggt121>
- Chin TL, Chen KY, Chen DY, Lin DE (2020) Intelligent real-time earthquake detection by recurrent neural networks. *IEEE Trans Geosci Remote Sens* 58(8):5440–5449. <https://doi.org/10.1109/TGRS.2020.2966012>
- Clement MA, Kilsby CG, Moore P (2018) Multi-temporal synthetic aperture radar flood mapping using change detection. *J Flood Risk Management* 11: 152–168. <https://doi.org/10.1111/jfr3.12303>
- Dong JJ, Tung YH, Chen CC, Liao JJ, Pan YW (2011) Logistic regression model for predicting the failure probability of a landslide dam. *Eng Geol* 117(1–2):52–61
- Ermini L, Casagli N (2003) Prediction of the behavior of landslide dams using geomorphological dimensionless index. *Earth Surf Process Landf* 28(1):31–47
- Fan X, Xu Q, Alonso-Rodriguez A et al (2019) Successive landsliding and damming of the Jinsha River in eastern Tibet, China: prime investigation, early warning, and emergency response. *Landslides* 16(5):1003–1020. <https://doi.org/10.1007/s10346-019-01159-x>
- Fei LY, Chen MM (2013) Geological investigation and database construction for upstream of flood-prone area – maps and explanatory text. Central Geological Survey, MOEA, Taiwan. 192pp
- Gimbert F, Fuller BM, Lamb MP, Tsai VC, Johnson JPL (2019) Particle transport mechanics and induced seismic noise in steep flume experiments with accelerometer-embedded tracers. *Earth Surf Process Landforms* 44:219–241. <https://doi.org/10.1002/esp.4495>
- Giustarini L, Hostache R, Matgen P et al (2013) A change detection approach to flood mapping in urban areas using TerraSAR-X. *IEEE TRANSACTIONS ON GEOSCIENCE AND REMOTE SENSING* 51(4):2417–2430. <https://doi.org/10.1109/TGRS.2012.2210901>
- Hanssen RF (2001) Radar interferometry: data interpretation and error analysis. Kluwer Academic Publisher, Dordrecht, Netherlands
- Lai VH, Tsai VC, Lamb MP, Ulizio TP, Beer AR (2018) The seismic signature of debris flows: flow mechanics and early warning at Montecito. *California Geophys Res Lett* 45:5528–5535. <https://doi.org/10.1029/2018GL077683>
- Lee K, Duncan J (1975) Landslide of April 25, 1974 on the Mantaro River, Peru. National Academy of Sciences, Washington, DC, 72
- Lin PS, Lee CT, Cheng CT, Sung CH (2011) Response spectral attenuation relations for shallow crustal earthquakes in Taiwan. *Eng Geol* 121:150–164
- Liu N, Chen Z, Zhang J, Lin W, Chen W, Xu W (2010) Draining the Tangjiashan barrier lake. *J Hydraul Eng* 136(11):914–923
- Mason DC, Speck R, Devereux B et al (2010) Flood detection in urban areas using TerraSAR-X. *IEEE TRANSACTIONS ON GEOSCIENCE AND REMOTE SENSING* 48(2):882–894. <https://doi.org/10.1109/TGRS.2009.2029236>
- Mason DC, Giustarini L, Garcia-Pintado J, Cloke HL (2014) Detection of flooded urban areas in high resolution synthetic aperture radar images using double scattering. *Int J Appl Earth Obs Geoinf* 28:150–159. <https://doi.org/10.1016/j.jag.2013.12.002>
- Manconi A, Picozzi M, Coviello V, de Santis F, Elia L (2016) Real time detection, location, and characterization of rockslides using broadband regional seismic networks. *Geophys Res Lett* 43:6960–6967. <https://doi.org/10.1002/2016GL069572>
- McNamara DE, Buland RP (2004) Ambient noise levels in the continental United States. *Bull Seismol Soc Am* 94(4):1517–1527
- Peng M, Zhang LM (2012) Breaching parameters of landslide dams. *Landslides* 9:13–31
- Polli P (2017) Creep and slip: seismic precursors to the Nuugaatsiaq landslide (Greenland). *Geophys Res Lett* 44:8832–8836
- Schmandt B, Aster RC, Scherler D, Tsai VC, Karlstrom K (2013) Multiple fluvial processes detected by riverside seismic and infrasound monitoring of a controlled flood in the Grand Canyon. *Geophys Res Lett* 40:4858–4863. <https://doi.org/10.1002/grl.50953>
- Schöpa A, Chao WA, Lipovsky BP et al (2018) Dynamics of the Askja caldera July 2014 landslide, Iceland, from seismic signal analysis: precursor, motion and aftermath. *Earth Surf Dynam* 6:467–485. <https://doi.org/10.5194/esurf-6-467-2018>
- Uddin K, Matin MA, Meyer FJ (2019) Operational flood mapping using multi-temporal Sentinel-1 SAR images: a case study from Bangladesh. *Remote Sensing* 11(13):1581. <https://doi.org/10.3390/rs11131581>
- Umbal JV, Rodolfo KS (1996) The 1991 lahars of southwestern Mount Pinatubo and evolution of the la-har-dammed Mapanuepe Lake. Fire and mud: eruptions and lahars of Mount Pinatubo, Philippines: Quezon, Philippine, 951–970
- Walder JS, O'Connor JE (1997) Methods of predicting peak discharge of floods caused by failure of natural and constructed earthen dams. *Water Resource Research* 33:2337–2348
- Walter F, Burtin A, McArdell BW et al (2017) Testing seismic amplitude source location for fast debris-flow detection at Illgraben. *Switzerland Nat Hazards Earth Syst Sci* 17:939–955. <https://doi.org/10.5194/nhess-17-939-2017>
- Weng MC, Lin CH, Shiu WJ, et al (2021) Towards a rapid assessment of highway slope disasters by using multidisciplinary techniques. *Landslides (minor revision)*
- Welch PD (1967) The use of fast Fourier transform for the estimation of power spectra: a method based on time averaging over short, modified periodograms. *IEEE TRANSACTIONS ON AUDIO AND ELECTROACOUSTICS* 15(2):70–73
- Wu W et al (2011) Earthen embankment breaching. *J Hydraul Eng* 137:1549–1564. [https://doi.org/10.1061/\(ASCE\)HY.1943-7900.0000498](https://doi.org/10.1061/(ASCE)HY.1943-7900.0000498)
- Yamada M, Kumagai H, Matsushi Y, Matsuzawa T (2013) Dynamic landslide processes revealed by broadband seismic records. *Geophys Res Lett* 40:2998–3002
- Yang CM, Kang KH, Yang SH et al (2020) Large paleo-rockslide induced by buckling failure at Jiasian in Southern Taiwan. *Landslides* 17(6):1319–1335

Supplementary Information The online version contains supplementary material available at <https://doi.org/10.1007/s10346-021-01818-y>.

### **Che-Ming Yang**

Department of Civil and Disaster Prevention Engineering, National United University, Miaoli 36063, Taiwan

### **Jui-Ming Chang**

Department of Geosciences, National Taiwan University, Taipei 10617, Taiwan

### **Chi-Yao Hung**

Department of Soil and Water Conservation, National Chung Hsing University, Taichung 40227, Taiwan

### **Chih-Heng Lu**

Research Center for Environmental Changes, Academia Sinica, Nankang 11529, Taiwan

### **Wei-An Chao** (✉) · **Keng-Hao Kang**

Department of Civil Engineering, National Yang Ming Chiao Tung University, Hsinchu 30010, Taiwan  
Email: vvnchao@gmail.com

### **Wei-An Chao** · **Keng-Hao Kang**

Disaster Prevention and Water Environment Research Center, National Yang Ming Chiao Tung University, Hsinchu 30010, Taiwan  
Email: vvnchao@gmail.com

### **Keng-Hao Kang**

He Yu Engineering Consultants Co., Ltd, Taichung 80424, Taiwan